

Article

Soft Chemistry Synthesis and Characterization of $\text{CoFe}_{1.8}\text{RE}_{0.2}\text{O}_4$ ($\text{RE}^{3+} = \text{Tb}^{3+}, \text{Er}^{3+}$) Ferrite

Dana Gingasu ^{1,*}, Ioana Mindru ¹, Adelina-Carmen Ianculescu ², Lucian Diamandescu ³, Vasile-Adrian Surdu ², Gabriela Marinescu ¹, Cristina Bartha ³, Silviu Preda ¹, Marcela Popa ⁴ and Mariana Carmen Chifiriuc ⁴

¹ “Ilie Murgulescu” Institute of Physical Chemistry, Romanian Academy, Splaiul Independentei 202, 060021 Bucharest, Romania; imandru@yahoo.com (I.M.); gabriela_marinescu02@yahoo.com (G.M.); predas01@yahoo.co.uk (S.P.)

² Faculty of Chemistry, “Politehnica” University of Bucharest, Polizu Street, No. 1–7, 011061 Bucharest, Romania; a_ianculescu@yahoo.com (A.-C.I.); adrian.surdu@live.com (V.-A.S.)

³ National Institute of Materials Physics, Atomistilor Street, No. 405 A, 077125 Magurele, Romania; ldiamandescu@gmail.com (L.D.); cristina.bartha@infim.ro (C.B.)

⁴ Microbiology Department, Faculty of Biology & Life, Environmental and Earth Sciences Division, Research Institute of the University of Bucharest, ICUB, University of Bucharest, Splaiul Independentei 91–95, 050095 Bucharest, Romania; bmarcelica@yahoo.com (M.P.); carmen_balotescu@yahoo.com (M.C.C.)

* Correspondence: d_gingasu@yahoo.com or dgingasu@icf.ro

Abstract: Nanosized $\text{CoFe}_{1.8}\text{RE}_{0.2}\text{O}_4$ ($\text{RE}^{3+} = \text{Tb}^{3+}, \text{Er}^{3+}$) ferrites were obtained through wet ferritization method. These ferrites were characterized by X-ray diffraction (XRD), scanning electron microscopy (FE-SEM), transmission electron microscopy (TEM/HR-TEM), Fourier transform infrared spectroscopy (FTIR), Mössbauer spectroscopy and magnetic measurements. The XRD results revealed that the average crystallite size is 5.77 nm for $\text{CoFe}_{1.8}\text{Tb}_{0.2}\text{O}_4$ and 6.42 nm for $\text{CoFe}_{1.8}\text{Er}_{0.2}\text{O}_4$. Distribution of metal cations in the spinel structure estimated from X-ray diffraction data showed that the Tb^{3+} and Er^{3+} ions occupy the octahedral sites. TEM images indicated the presence of polyhedral particles with average size 5.91 nm for $\text{CoFe}_{1.8}\text{Tb}_{0.2}\text{O}_4$ and 6.80 nm for $\text{CoFe}_{1.8}\text{Er}_{0.2}\text{O}_4$. Room temperature Mössbauer spectra exhibit typical nanoscaled cobalt ferrite spectra in good agreement with XRD and TEM data. The saturation magnetization value (M_s) is 60 emu/g for $\text{CoFe}_{1.8}\text{Tb}_{0.2}\text{O}_4$ and 80 emu/g for $\text{CoFe}_{1.8}\text{Er}_{0.2}\text{O}_4$. $\text{CoFe}_{1.8}\text{RE}_{0.2}\text{O}_4$ nanoparticles showed similar antimicrobial efficacy against the five tested microbial strains, both in planktonic and biofilm state. The results highlight the promising potential of these types of nanoparticles for the development of novel anti-biofilm agents and materials.

Keywords: nanospinel ferrites; wet chemical method; magnetic properties; antimicrobial activity



Citation: Gingasu, D.; Mindru, I.; Ianculescu, A.-C.; Diamandescu, L.; Surdu, V.-A.; Marinescu, G.; Bartha, C.; Preda, S.; Popa, M.; Chifiriuc, M.C. Soft Chemistry Synthesis and Characterization of $\text{CoFe}_{1.8}\text{RE}_{0.2}\text{O}_4$ ($\text{RE}^{3+} = \text{Tb}^{3+}, \text{Er}^{3+}$) Ferrite. *Magnetochemistry* **2022**, *8*, 12. <https://doi.org/10.3390/magnetochemistry8020012>

Academic Editor: Andrea Caneschi

Received: 15 December 2021

Accepted: 15 January 2022

Published: 19 January 2022

Publisher’s Note: MDPI stays neutral with regard to jurisdictional claims in published maps and institutional affiliations.



Copyright: © 2022 by the authors. Licensee MDPI, Basel, Switzerland. This article is an open access article distributed under the terms and conditions of the Creative Commons Attribution (CC BY) license (<https://creativecommons.org/licenses/by/4.0/>).

1. Introduction

In recent decades, spinel ferrite and substituted spinel ferrite nanoparticles have attracted an increasing interest due to their potential applications in several fields, such as permanent magnets, microwave devices, information storage systems, magnetic fluids and magnetic soft robots [1–3]. In terms of biomedical applications, they are used for diagnosis (magnetic resonance imaging, biosensors) and treatment (e.g., cancer treatment, drug delivery systems, magnetic hyperthermia) [4–8]. The properties of these ferrites are dependent on the nature of the cations, their charges and their distribution between the tetrahedral (A) and the octahedral (B) sublattices of the spinel structure [9].

Cobalt ferrite (CoFe_2O_4), an important member of the spinel family, crystallizes in a partially inverse spinel structure, $(\text{Co}_{1-\lambda}^{2+} \text{Fe}_{\lambda}^{3+})_A [\text{Co}_{\lambda}^{2+} \text{Fe}_{2-\lambda}^{3+}]_B \text{O}_4$, where λ is the degree of inversion and it depends on the preparation conditions and thermal history [10]. CoFe_2O_4 is ferrimagnetic with a Curie temperature (T_c) around 520 °C, large anisotropy and moderate saturation magnetization, as well as tunable coercivity; it exhibits physical and chemical stability [11].

Several reports have been published on the effect of the substitution of Co^{2+} in cobalt ferrite with rare earth and transition metal ions [12–15]. The presence of rare earth (RE) elements influences its structural and magnetic properties [12]. The large ionic radii and highly localized magnetic moments of 4f electrons of the lanthanides is expected to influence the anisotropy due to the strong spin-orbit coupling and also to cause structural distortion [13,14].

Over the past decade, some studies revealed the antimicrobial activity of the cobalt ferrite and substituted cobalt ferrite nanoparticles, $\text{M}_x\text{Co}_{1-x}\text{Fe}_2\text{O}_4$ ($\text{M} = \text{Zn}, \text{Cu}, \text{Mn}$), on pathogenic and multidrug resistant bacterial strains [15–19]. An overview of the literature shows also studies on the antimicrobial properties of rare earth substituted cobalt ferrite nanoparticles $\text{CoFe}_{2-x}\text{RE}_x\text{O}_4$ ($\text{RE}^{3+} = \text{La}^{3+}, \text{Dy}^{3+}, \text{Yb}^{3+}, \text{Gd}^{3+}, \text{Ce}^{3+}$) [20,21].

The proper choice of the synthesis method will play an important role on the composition, structure and morphology of the oxides, influencing also their biological activities, including antimicrobial activity. Žalnėravičius et al. [20] have studied the influence of the nanoparticle size on the antimicrobial activity and have reported that this activity was increased with the decreasing of the particle size.

Rare earth substituted ferrite nanoparticles were synthesized by various methods such as the coprecipitation method [9,21,22], the combustion techniques [12,14,23], the microemulsion method [10], the forced hydrolysis in polyol [24] and the sonochemical method [13].

The literature of the last decade shows that there are only few studies relating to Er- and Tb-doped cobalt ferrite. Wu et al. [25] prepared $\text{CoFe}_{1.9}\text{Tb}_{0.1}\text{O}_4$ nanoparticles via hydrothermal method, with the average crystallite sizes of 14 nm and saturation magnetization of 58 emu/g. The adsorption capacity of Congo Red onto $\text{CoFe}_{1.9}\text{Tb}_{0.1}\text{O}_4$ sample is 142.5 mg/g at contact time of 90 min. This indicates that the obtained material is a promising adsorbent for dye removal from wastewater. Ateia et al. [12] used citrate autocombustion method to obtain $\text{CoFe}_{1.975}\text{Er}_{0.025}\text{O}_4$ with average crystallite size of 11 nm and saturation magnetization of 59 emu/g. The study by Sumalatha et al. [26] has shown that Er^{3+} doping in CoFe_2O_4 ($\text{CoEr}_x\text{Fe}_{2-x}\text{O}_4$, where $x = 0.005\text{--}0.030$) resulted in the decline of magnetic parameters. The samples, obtained by citrate-gel auto combustion technique, have crystallite sizes in the range of 20–14 nm and saturation magnetization in 58–44 emu/g range. Moreover, the obtained Er-doping cobalt ferrites can be used in electromagnetic applications due to the presence of magnetic dipole.

We hereby report a wet chemical method—so-called “the wet ferritization method”—that takes place in a single step at low temperature [17,27]. This method—a chemical synthesis route belonging to the soft chemistry—implies the decomposition of the polynuclear coordination compounds directly in the reaction medium.

The aim of this work was the synthesis of $\text{CoFe}_{1.8}\text{RE}_{0.2}\text{O}_4$ ($\text{RE}^{3+} = \text{Tb}^{3+}, \text{Er}^{3+}$) ferrite nanoparticles and the investigation of the structural, morphological and magnetic properties. The antimicrobial activity of the obtained samples against several bacterial and fungal strains, in planktonic and biofilm growth state was investigated.

2. Experimental

2.1. Reagents

Iron(III) nitrate ($\text{Fe}(\text{NO}_3)_3 \cdot 9\text{H}_2\text{O}$), cobalt(II) nitrate ($\text{Co}(\text{NO}_3)_2 \cdot 6\text{H}_2\text{O}$), terbium(III) nitrate ($\text{Tb}(\text{NO}_3)_3 \cdot 6\text{H}_2\text{O}$) and erbium(III) nitrate ($\text{Er}(\text{NO}_3)_3 \cdot 5\text{H}_2\text{O}$), all of reagent quality (Merck), were used as received in the synthesis procedure. The ammonia solution 25% was purchased from Chimreactiv, Romania.

2.2. Synthesis of $\text{CoFe}_{1.8}\text{RE}_{0.2}\text{O}_4$ ($\text{RE}^{3+} = \text{Tb}^{3+}, \text{Er}^{3+}$)

The metal nitrates (in the molar ratio $1.8\text{Fe}^{3+}:1\text{Co}^{2+}:0.2\text{RE}^{3+}$) were dissolved under stirring in distilled water. After the addition of the precipitating agent (25% NH_4OH) and raising the pH to 10, a dark brown compound precipitated. This suspension was maintained 7 h at 80 °C and the dark precipitate became magnetic. After filtering and

washing with distilled water, the precipitate was dried on P_4O_{10} . A cobalt ferrite ($CoFe_2O_4$) has been obtained in the same manner [17].

2.3. Characterization Techniques

Powder X-ray diffraction investigations were performed by using a Rigaku Ultima IV diffractometer in a parallel beam geometry, equipped with $CuK\alpha$ radiation ($\lambda = 1.5406 \text{ \AA}$), Cross Beam Optics (CBO) and graphite monochromator, and operated at 40 kV and 30 mA. The measurements were performed in 2θ range, between 10° and 80° with a scanning rate of 5° min^{-1} and a scan step increment of 0.02° . Phase identification was done by using the HighScore Plus 3.0e software, connected to the ICDD PDF-4+2017 database. The corresponding unit cell and space group were determined using McMaille method and full profile Le Bail fit, assuming that all RE^{3+} ions occupy the octahedral sublattice, 16d Wychoff position. Lattice parameters were then refined by the Rietveld method. After removing the instrumental contribution, the full-width at half-maximum (FWHM) of the diffraction peaks can be interpreted in terms of crystallite size and lattice strain. A Pseudo-Voigt function was used to refine the shapes of the $CoFe_{1.8}RE_{0.2}O_4$ peaks and a Caglioti function was used for FWHM approximation. Unit cell parameter, a , and oxygen occupancy, u , were used to determine the cation radii [28]:

$$r_T = a\sqrt{3}(u - 0.125) - r_{O^{2-}} \quad (1)$$

$$r_O = a\sqrt{3u^2 - 2u + 0.375} - r_{O^{2-}} \quad (2)$$

where r_T and r_O are the average cation radius of the tetrahedral sublattice and octahedral sublattice, respectively.

The inversion degree λ was estimated according to O'Neill method [29]:

$$\langle r_T \rangle = (1 - \lambda)(r_{Co^{2+},t}) + \lambda(r_{Fe^{3+},t}) \quad (3)$$

$$\langle r_O \rangle = \frac{\lambda(r_{Co^{2+},o}) + (1.8 - \lambda)(r_{Fe^{3+},o}) + 0.2(r_{Ln^{3+},o})}{2} \quad (4)$$

where λ , the degree of inversion, is the fraction of tetrahedral A sites occupied by Fe^{3+} and $(r_{X^{n+},s})$ are the effective cation radii as expressed by Shannon [30].

The microstructure of the $CoFe_{1.8}RE_{0.2}O_4$ powder samples was studied by scanning electron microscopy (FE-SEM), using a high resolution FEI QUANTA INSPECT F microscope with field emission gun. The transmission electron microscopy (TEM/HR-TEM) and selected area electron diffraction (SAED) analyses were performed by means a TecnaiTM G² F30 S-TWIN transmission electron microscope, coupled with energy-dispersive X-ray spectroscopy (EDX) component to investigate the elemental composition. The average particle size for the $CoFe_{1.8}RE_{0.2}O_4$ powder samples was determined using the OriginPro 9.0 software by taking into account size measurements on 50–60 particles from TEM images of appropriate magnifications obtained from various microscopic fields. The TEM specimens were prepared by dispersion of the ferrite powders in ethanol by ultrasonication and deposition of the resulting suspension onto a 400 mesh, holey carbon coated film copper grid, and dried.

Fourier transform infrared (FTIR) spectra were recorded on KBr pellets by a JASCO FTIR 4100 spectrophotometer in the frequency range of $4000\text{--}400 \text{ cm}^{-1}$.

Mössbauer spectra were recorded at room temperature using a WissEL-ICE Oxford cryomagnetic system and a 10 mCi Co in the rhodium matrices source. In order to avoid additional contributions to the line width, the sample thickness was calculated at $\sim 5 \text{ mg cm}^{-2}$. The velocity calibration was performed with a standard $\alpha\text{-Fe}$ foil. The spectra were computed in the hypothesis of Lorentzian line shape.

The magnetization versus field measurements were carried out using a MPMS SQUID magnetometer (Quantum Design) at two different temperatures (5 and 300 K) and an applied magnetic field up to 5 Tesla.

2.4. Bioevaluation of the Obtained Nanoparticles

The antimicrobial activity of the obtained nanoparticles was evaluated on Gram-negative (*Escherichia coli* ATCC 8739, *Pseudomonas aeruginosa* ATCC 27853), Gram-positive (*Staphylococcus aureus* ATCC 6538, *Enterococcus faecalis* ATCC 29212) and fungal (*Candida albicans* ATCC 10231) strains. The used quantitative assays allowed to establish the minimal inhibitory concentration (MIC), indicating the efficiency against planktonic cells and the minimal biofilm eradication concentration (MBEC), showing the anti-biofilm potential of the respective nanoparticles. In this purpose, a stock suspension of 10 mg mL^{-1} in dimethyl sulfoxide (DMSO) was used to perform serial binary dilutions, ranging from 1 mg to 0.002 mg mL^{-1} , in $200 \mu\text{L}$ of Muller Hinton broth distributed in 96-well microplates. The respective microplates were then inoculated with microbial suspensions of 0.5 McFarland density (corresponding to $1.5 \times 10^8 \text{ CFU mL}^{-1}$). Positive (microbial suspensions) and negative (sterile culture medium) controls were used. After incubation at 37°C for 24 h, the absorbance of the liquid cultures was read at 600 nm (Apollo LB 911 ELISA reader). The MIC value was considered as the lowest concentration of the tested nanoparticles that inhibited the planktonic growth, the absorbance value being comparable to that of the negative control.

After the MIC reading, the plates were emptied, and the biofilms adhered to the plastic wells were fixed for 5 min with cold methanol, colored for 15 min with violet crystal and then resuspended with acetic acid 33%. The MBEC value was established by measuring the optical density of the colored suspension at 490 nm and corresponded to the lowest concentration of the tested nanoparticles that inhibited the development of microbial biofilm [31].

3. Results and Discussion

3.1. Structural Characterization

The XRD diffraction patterns of $\text{CoFe}_{2-x}\text{RE}_x\text{O}_4$ ($\text{RE}^{3+} = \text{Tb}^{3+}, \text{Er}^{3+}$) powder samples indicated the complete incorporation of the solutes into the CoFe_2O_4 lattice with the formation of the single phase cubic spinel structure, belonging to the space group Fd3m (Figure 1). This means that, for a substitution degree corresponding to $x = 0.2$, the solubility limit of Tb^{3+} , as well as that one of Er^{3+} on the octahedral B sites of the spinel network is not yet reached. These results are not consistent with those reported previously by Kakade et al. [32] and Prathapani et al. [14], who have found lower values of the solubility limit corresponding to $x < 0.15$ and $x < 0.03$, respectively, in Er^{3+} -doped cobalt ferrite powders prepared by the sol-gel combustion method. On the other hand, our results are in agreement with those reported by Cheng et al. [33] for their Er^{3+} -doped cobalt ferrite films prepared via sol-gel method. One can conclude that the spread of the data regarding the solubility of RE^{3+} ions in the spinel structure of CoFe_2O_4 is related to the preparation route and, for a similar preparation method, it strongly depends on the synthesis/thermal processing factors. In our case, the best fit was obtained by using the ICDD card no. 01-080-6487, corresponding to CoFe_2O_4 . When Fe^{3+} ions onto the octahedral sites (C.N. = 6) are partially replaced by $\text{Tb}^{3+}/\text{Er}^{3+}$ ions, an increase in the lattice parameter values is expected, taking into account the values of the ionic radii of the substituting and substituted species, i.e., $r(\text{Tb}^{3+}) = 0.923 \text{ \AA}$ and $r(\text{Er}^{3+}) = 0.89 \text{ \AA}$, relative to the Fe^{3+} ionic radius in high spin state, $r(\text{Fe}^{3+}) = 0.645 \text{ \AA}$ [30]. Indeed, the lattice parameter a increases and, consequently, the unit cell slightly expands in the order $\text{CoFe}_2\text{O}_4 < \text{CoFe}_{1.8}\text{Er}_{0.2}\text{O}_4 < \text{CoFe}_{1.8}\text{Tb}_{0.2}\text{O}_4$. On the other hand, due to the higher atomic mass of erbium and terbium solutes, relative to the atomic mass of the substituted iron host-specie, the molecular mass of $\text{CoFe}_{1.8}\text{RE}_{0.2}\text{O}_4$ becomes significantly higher than that one corresponding to the un-doped CoFe_2O_4 . In the case of the RE^{3+} -doped compositions, the increase rate of molecular mass due to

the presence of heavy metals is faster than that of the volume of the unit cell, so that the crystallographic (theoretical) density values decrease in the order $\text{CoFe}_{1.8}\text{Er}_{0.2}\text{O}_4 > \text{CoFe}_{1.8}\text{Tb}_{0.2}\text{O}_4 > \text{CoFe}_2\text{O}_4$.

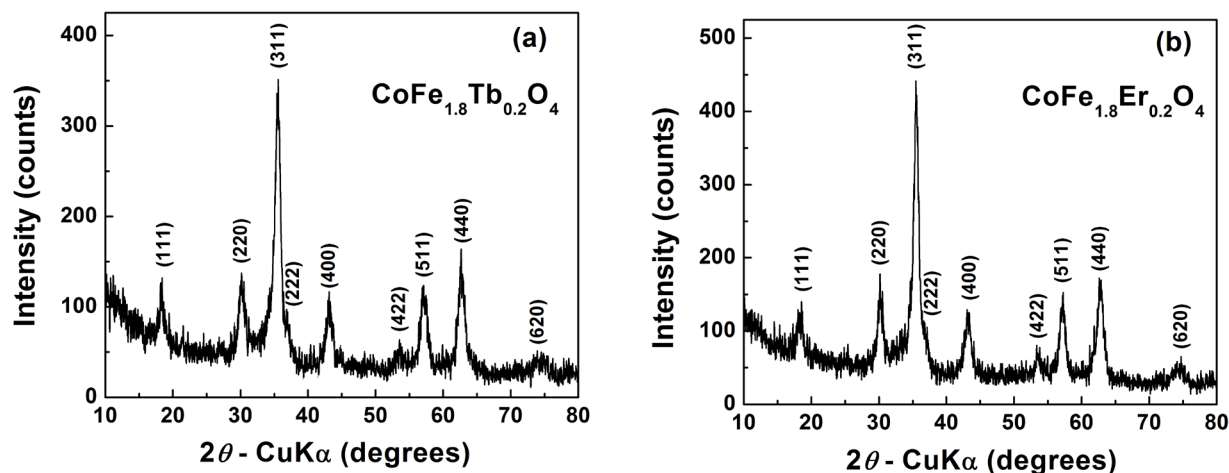


Figure 1. XRD patterns of spinel ferrites: (a) $\text{CoFe}_{1.8}\text{Tb}_{0.2}\text{O}_4$ sample; (b) $\text{CoFe}_{1.8}\text{Er}_{0.2}\text{O}_4$ sample.

The increase in the mismatch of the ionic radii values of RE^{3+} solutes, and Fe^{3+} host cations induce a slight decrease of the average crystallite size and, concurrently, a slight increase of the lattice microstrains. The values of the structural parameters are summarized in Table 1. It is worthy to mention that our results are in good agreement with the data reported by Kakade et al. [32] who also found an increase in the unit cell parameter and the reduction in the crystallite size with the increase of the erbium content in their Er^{3+} -substituted nanocrystalline, cobalt-rich ferrite samples prepared by sol-gel autocombustion method.

Table 1. Structural and microstructural parameters of CoFe_2O_4 (from ICDD 01-080-6487) and synthesized $\text{CoFe}_{1.8}\text{Er}_{0.2}\text{O}_4$ and $\text{CoFe}_{1.8}\text{Tb}_{0.2}\text{O}_4$ powder samples.

Structural/Microstructural Parameters	Composition		
	CoFe_2O_4 (ICDD 01-080-6487)	$\text{CoFe}_{1.8}\text{Er}_{0.2}\text{O}_4$	$\text{CoFe}_{1.8}\text{Tb}_{0.2}\text{O}_4$
Unit cell parameters (cubic Fd3m)			
$a = b = c$ (Å)	8.3554	8.3751 ± 0.0051	8.3775 ± 0.0018
$\alpha(\circ) = \beta(\circ) = \gamma(\circ)$	90	90	90
No. molecules/unit cell, Z	8	8	8
Unit cell volume, V (Å ³)	583.31	587.45	587.95
Oxygen occupancy, u	0.25664	0.258455	0.260472
Average cation radius of the tetrahedral sublattice, r_T (Å)	0.5251	0.5559	0.5857
Average cation radius of the octahedral sublattice, r_O (Å)	0.6549	0.64545	0.6305
Theoretical density, ρ_t (g/cm ³)	5.343	5.809	5.766
Average crystallite size, $\langle D \rangle$ (nm)	-	6.42 ± 0.63	5.77 ± 0.50
Microstrains (%)	-	1.41 ± 0.54	1.57 ± 0.62
Degree of inversion	0.61	0.25	0
Formula obtained for the estimated degree of inversion, λ	$(\text{Co}_{0.39}^{2+}\text{Fe}_{0.61}^{3+})_T[\text{Co}_{0.61}^{2+}\text{Fe}_{1.39}^{3+}]_O\text{O}_4$	$(\text{Co}_{0.75}^{2+}\text{Fe}_{0.25}^{3+})_T[\text{Co}_{0.25}^{2+}\text{Fe}_{1.55}^{3+}\text{Er}_{0.2}^{3+}]_O\text{O}_4$	$(\text{Co}^{2+})_T[\text{Fe}_{1.8}^{3+}\text{Tb}_{0.2}^{3+}]_O\text{O}_4$
Goodness of fit, χ^2	-	2.34845	1.49297
Average particle size, $\langle d_{\text{TEM}} \rangle$ (nm)	-	6.80 ± 1.81	5.91 ± 2.13

In a spinel structure, the degree of inversion represents the fraction of tetrahedral sites occupied by B ions. Therefore, in CoFe_2O_4 the degree of inversion, λ , is related to the fraction of Co^{2+} ions which occupy the tetrahedral sites of the spinel structure with the general formula $(\text{Co}_{1-\lambda}^{2+}\text{Fe}_{\lambda}^{3+})_T[\text{Co}_{\lambda}^{2+}\text{Fe}_{2-\lambda}^{3+}]_O\text{O}_4$. The calculated value of the degree of

inversion $\lambda = 0.61$, obtained for the pure CoFe_2O_4 from ICDD card no. 01-080-6487, shows that Co^{2+} cations are not found entirely onto the octahedral sites of the spinel lattice, as in a typical inverse spinel, but a certain fraction ($1 - \lambda = 0.39$) also occupies the tetrahedral sites. As a result, the fraction of Fe^{3+} ions on the octahedral sites is higher than in an ideal inverse spinel with the theoretical formula $(\text{Fe}^{3+})_{\text{T}}[\text{Co}^{2+}\text{Fe}^{3+}]_{\text{O}}\text{O}_4$.

It is well-known that RE^{3+} species exhibit a high tendency to occupy the octahedral site because of their larger ionic radius than that of the host metal ions on the octahedral B site ($r(\text{Co}^{2+}) = 0.745 \text{ \AA}$ and $r(\text{Fe}^{3+}) = 0.645 \text{ \AA}$) [34]. It seems very likely that the entrance of the larger Tb^{3+} and Er^{3+} cations into the octahedral sites of the spinel lattice induces internal strains which are released by the partial migration of Co^{2+} ions from octahedral to tetrahedral sites, concurrently with the opposite migration of an equal fraction of smaller Fe^{3+} ions from the tetrahedral toward the octahedral sites. The higher ionic radius value of the RE^{3+} solute, the lower will be the degree of inversion, i.e., the stronger will be the preference of Co^{2+} ions for a tetrahedral coordination. Consequently, for the composition $\text{CoFe}_{1.8}\text{Er}_{0.2}\text{O}_4$, the inversion degree decreases to a λ value of 0.25, while in the $\text{CoFe}_{1.8}\text{Tb}_{0.2}\text{O}_4$ sample, the presence of the larger Tb^{3+} ions determines a clear evolution toward a normal spinel structure ($\lambda = 0$) (Table 1). This tendency of cobalt ions reordering from the octahedral sites (B) to the tetrahedral sites (A) was also reported by Naik and Salker [35] for a significantly lower Dy^{3+} amount ($x = 0.03$) incorporated in CoFe_2O_4 lattice of their sample synthesized by sol-gel assisted autocombustion. However, in order to better clarify the influence of RE^{3+} ions on the site occupancy of cations in the substituted cobalt ferrite, these results should be sustained by experimental data provided by more powerful experimental tools, as neutron diffraction. Two factors: particle size of ferrite and size of dopant RE^{3+} ion contribute to the level of internal microstrains in substituted cobalt ferrite. Taking into account their opposite influence, the slightly higher value of internal strains in $\text{CoFe}_{1.8}\text{Tb}_{0.2}\text{O}_4$ (Table 1) seems to indicate that the effect determined by a lower particle size prevails over the effect of the larger Tb^{3+} ions in inducing a higher structural relaxation by reducing the degree of inversion.

3.2. FE-SEM and TEM/HRTEM Investigations

FE-SEM investigations revealed that both $\text{CoFe}_{1.8}\text{Tb}_{0.2}\text{O}_4$ and $\text{CoFe}_{1.8}\text{Er}_{0.2}\text{O}_4$ powders consist of particles with sizes in the nanometric range, which exhibit a high agglomeration tendency, so that even a rough estimation of the average particle size becomes a difficult task (Figure 2a,b).

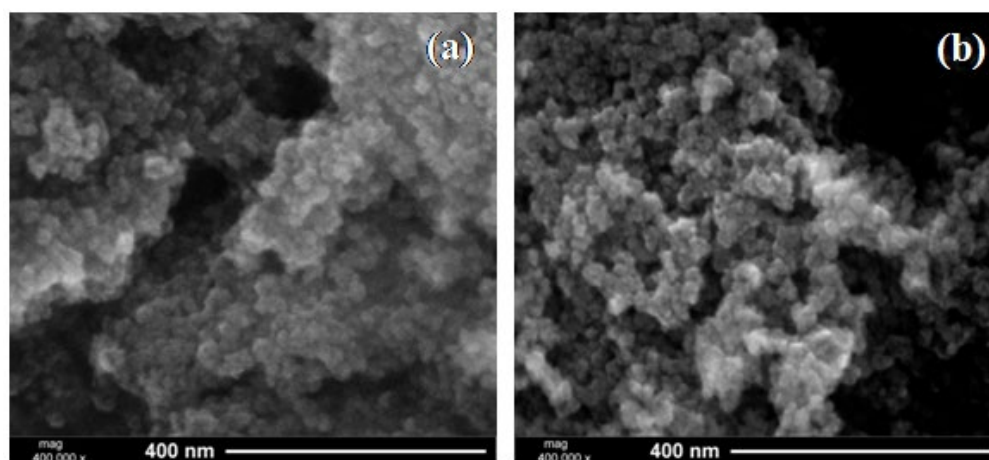


Figure 2. FE-SEM images of: (a) $\text{CoFe}_{1.8}\text{Tb}_{0.2}\text{O}_4$ powder sample; (b) $\text{CoFe}_{1.8}\text{Er}_{0.2}\text{O}_4$ powder sample.

In order to overcome this drawback and to estimate more accurately the size and details regarding the shape of the particles, TEM analyses were performed. The TEM images (Figures 3a and 4a) show that, both, $\text{CoFe}_{1.8}\text{Tb}_{0.2}\text{O}_4$ and $\text{CoFe}_{1.8}\text{Er}_{0.2}\text{O}_4$ consist of primary polyhedral particles, with sizes below 10 nm. The determined average particle

size ($\langle d_{\text{TEM}} \rangle$) is 5.91 nm for the $\text{CoFe}_{1.8}\text{Tb}_{0.2}\text{O}_4$ powder and 6.80 nm for the $\text{CoFe}_{1.8}\text{Er}_{0.2}\text{O}_4$ sample, as revealed the related particle size distribution histograms (insets of Figures 3a and 4a). These values are close to those corresponding to the average crystallite size presented in Table 1, which suggest the single-crystal nature of $\text{CoFe}_{1.8}\text{RE}_{0.2}\text{O}_4$ particles under investigation. The size of these particles, synthesized by the wet ferritization method, is significantly lower than the sizes reported for RE^{3+} -substituted CoFe_2O_4 powders prepared by other wet chemical routes, as the sol-gel assisted auto-combustion method [32,36].

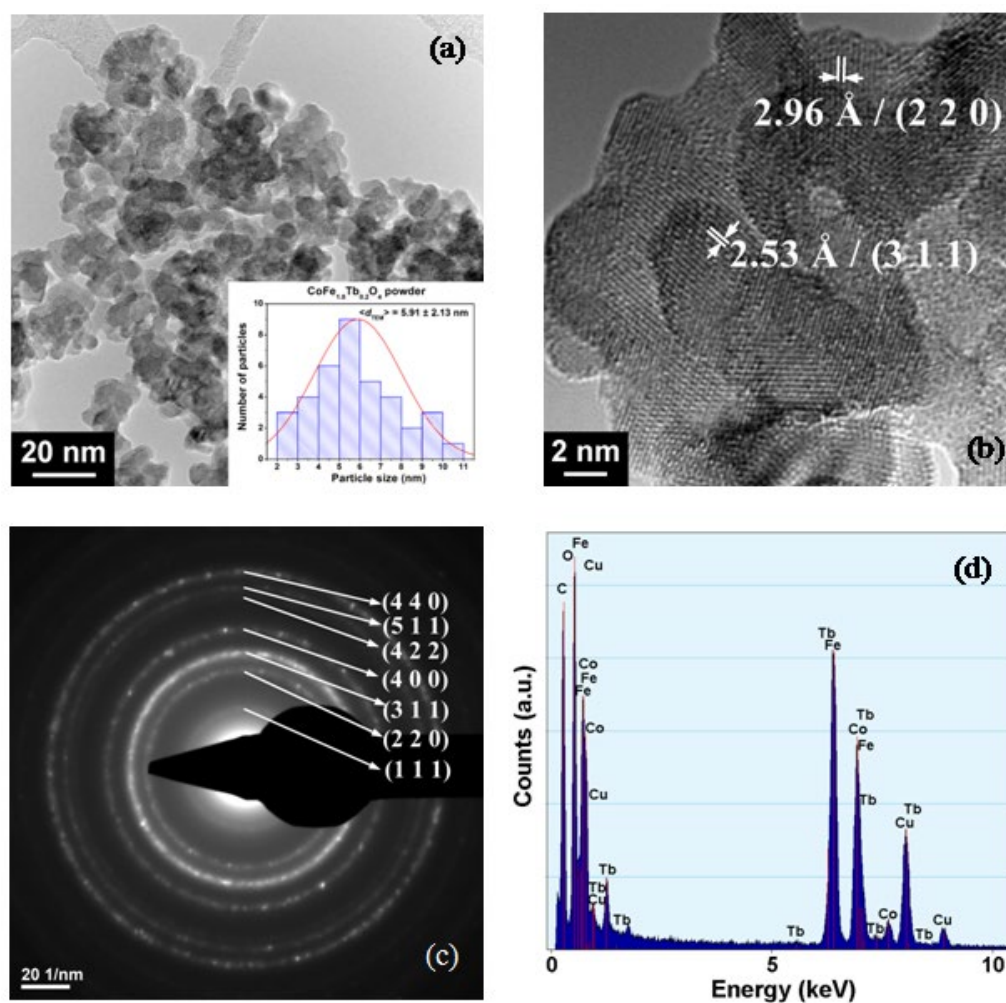


Figure 3. (a) TEM image and histogram showing the particle size distribution obtained from the related TEM images (inset); (b) HRTEM image; (c) selected area electron diffraction pattern; (d) EDX spectrum of $\text{CoFe}_{1.8}\text{Tb}_{0.2}\text{O}_4$ powder sample.

The HRTEM images (Figures 3b and 4b) revealed the presence, inside the well-crystallized particles, of long-range ordered fringes spaced at 2.96 Å and 2.53 Å, corresponding to the crystalline (2 2 0) and (3 1 1) planes of the spinel lattice. The clearly defined diffraction rings, without any halo specific to a potential amorphous phase, also suggest a high crystallinity, in spite of the nanometric size of both particle types. The purity of the powders was checked by qualitative EDX analyses. No contaminants were detected, so that the EDX spectra show only the host Co, Fe, Er, Tb and O elements (Figures 3d and 4d). The occurrence of the C peak in the spectra is determined by the carbon coating of the Cu grid used for the investigations.

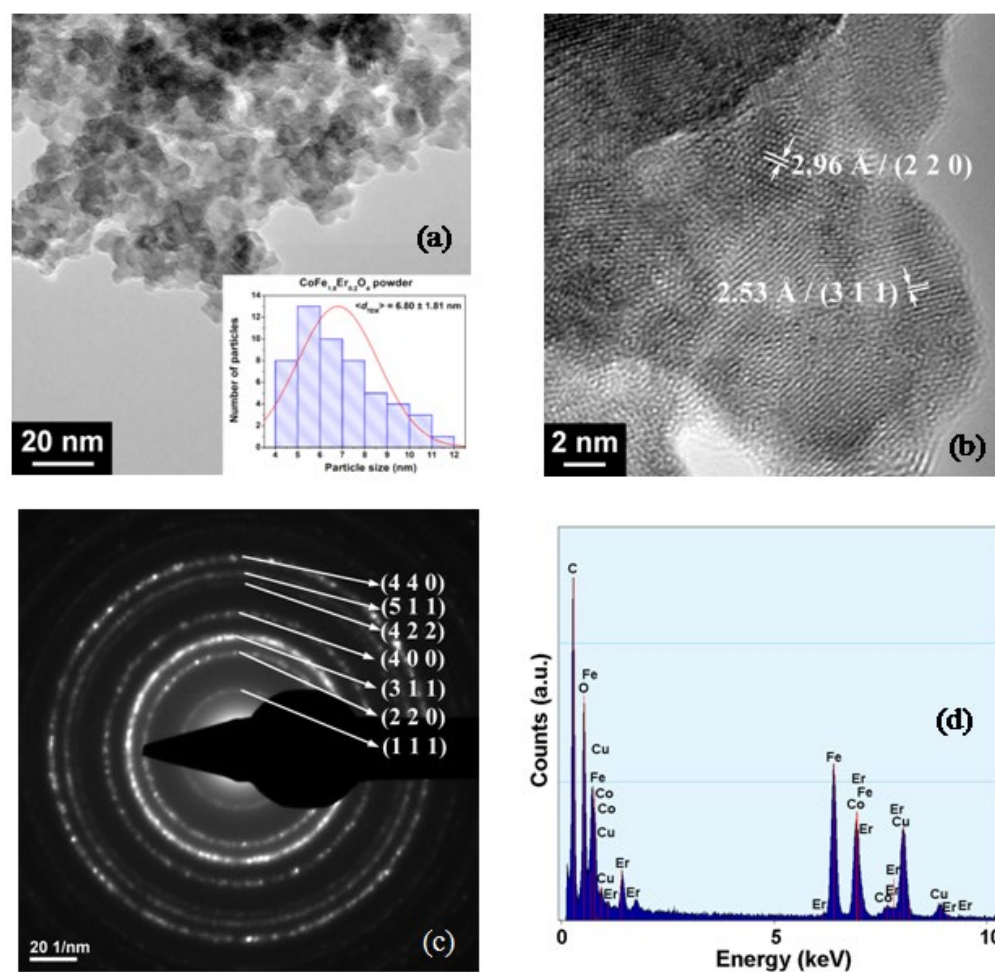


Figure 4. (a) TEM image and histogram showing the particle size distribution obtained from the related TEM images (inset); (b) HRTEM image; (c) selected area electron diffraction pattern; (d) EDX spectrum of $\text{CoFe}_{1.8}\text{Er}_{0.2}\text{O}_4$ powder sample.

3.3. FTIR Spectra

The formation of the spinel structure of $\text{CoFe}_{1.8}\text{RE}_{0.2}\text{O}_4$ ($\text{RE}^{3+} = \text{Tb}^{3+}, \text{Er}^{3+}$) is also supported by FTIR analysis (Figure 5). Two intense bands at about $570\text{--}580\text{ cm}^{-1}$ and $450\text{--}390\text{ cm}^{-1}$ were due to the stretching vibrations of Fe-O and Co-O in tetrahedral and octahedral sites, respectively [37]. The low intense bands between 1620 and 1370 cm^{-1} together with the broad band at about 3350 cm^{-1} have been assigned to the H-O-H bonding mode of adsorbed water molecules on the surface of the spinel oxides [38].

3.4. Mössbauer Spectroscopy

Room temperature Mössbauer spectra are presented in Figure 6A together with the computer fit (continuous lines) in the hypothesis of Lorentzian line. All spectra consist in a magnetic hyperfine pattern with very large and distorted shape accompanied by a central quadrupole contribution (red continuous line).

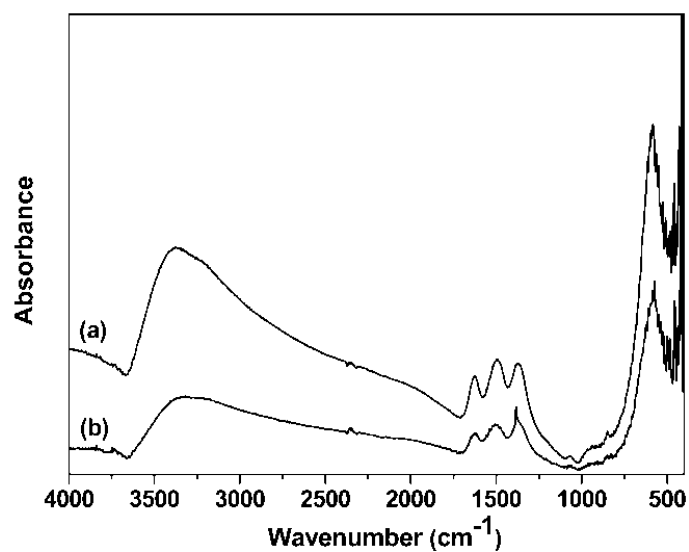


Figure 5. FTIR spectra of: (a) $\text{CoFe}_{1.8}\text{Tb}_{0.2}\text{O}_4$ powder sample; (b) $\text{CoFe}_{1.8}\text{Er}_{0.2}\text{O}_4$ powder sample.

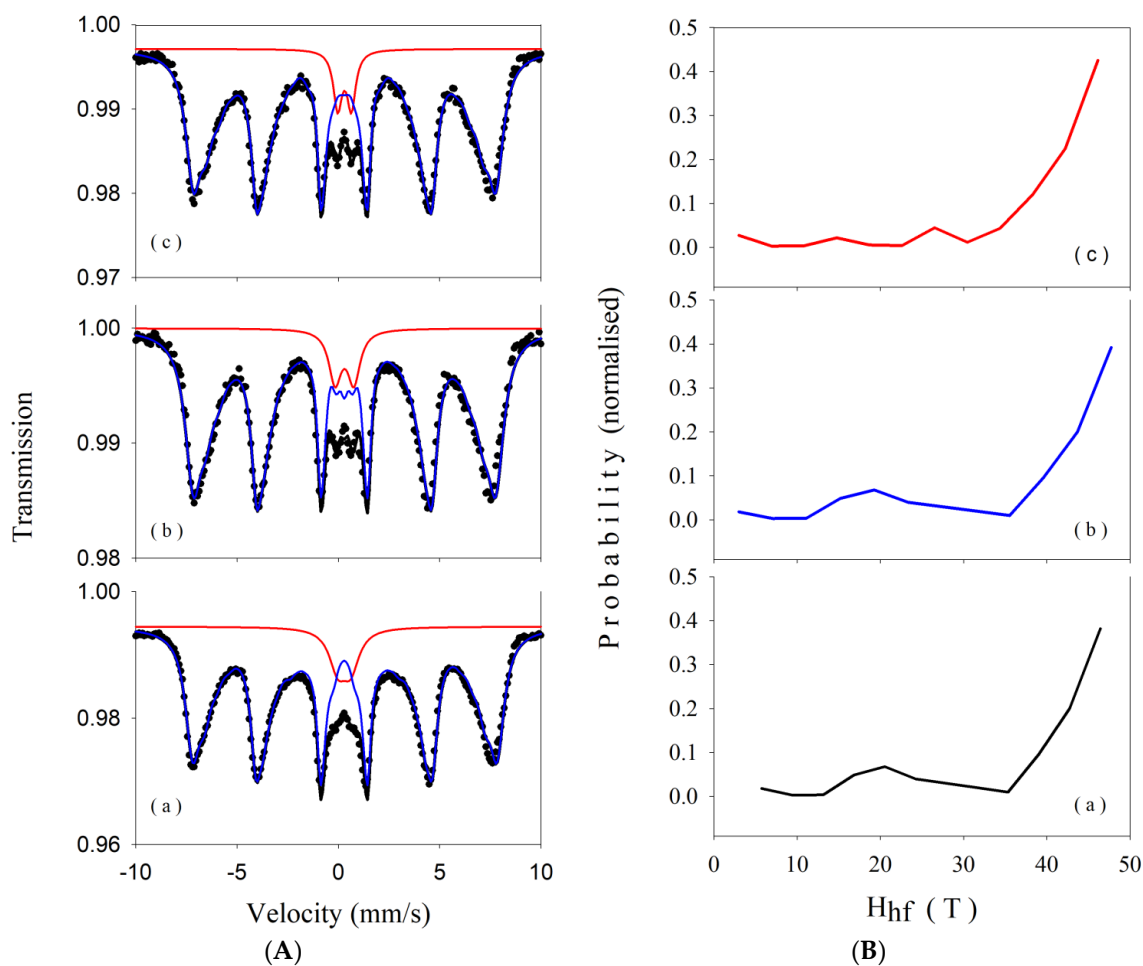


Figure 6. (A) Room temperature Mössbauer spectra of nanoscaled samples: (a) CoFe_2O_4 ; (b) $\text{CoFe}_{1.8}\text{Er}_{0.2}\text{O}_4$; (c) $\text{CoFe}_{1.8}\text{Tb}_{0.2}\text{O}_4$. (B) The distribution probabilities versus magnetic hyperfine field for the same samples: (a) CoFe_2O_4 ; (b) $\text{CoFe}_{1.8}\text{Er}_{0.2}\text{O}_4$; (c) $\text{CoFe}_{1.8}\text{Tb}_{0.2}\text{O}_4$.

In the case of bulk CoFe_2O_4 samples, the Mössbauer spectrum consists in two hyperfine magnetic sextets representing iron ions from the octahedral and tetrahedral sites [39].

The magnetic hyperfine fields at Mössbauer nucleus in tetrahedral and octahedral sites are generally of the order of ~49 T and ~51 T respectively, depending strongly of the preparation method and thermal history of the sample. The Mössbauer spectrum is a sum of contributions from iron ions in all samples. In the case of micro- and nano-scale powders, the hyperfine magnetic field at Mössbauer nucleus depends on particle size, decreasing with the decrease of particle volume [40], as shown by the following formula:

$$H_{\text{hf}}(V,T) = H_{\text{hf}}(V_{\text{bulk}},T) [1 - k_{\text{B}}T/2KV] \quad (5)$$

where V is the particle volume, k_{B} is the Boltzmann constant, K is the anisotropy constant and T is the temperature (K).

As shown by the above TEM investigations our samples exhibit a particle size distribution with maxima centered in the region of 5–7 nm. Therefore, our spectra will consist in a distribution of hyperfine magnetic fields reflecting the particle volume distribution as evidenced by TEM, accompanied by doublets or single lines—as contribution from very small particle to the Mössbauer spectrum. Figure 6B exhibits the distribution probabilities versus magnetic hyperfine field for all studied samples. No relevant differences can be observed from cobalt ferrite to Er or Tb substituted one, suggesting a crucial contribution of particle volume in the drop of hyperfine magnetic field.

Table 2 presents the main Mössbauer hyperfine parameters (IS—the isomer shift, ΔE_{Q} —the quadrupole splitting and H_{hf} —the magnetic hyperfine field at Mössbauer nucleus of the analyzed samples).

Table 2. Mössbauer fit parameters of nanoscaled spinels: CoFe_2O_4 , $\text{CoFe}_{1.8}\text{Er}_{0.2}\text{O}_4$ and $\text{CoFe}_{1.8}\text{Tb}_{0.2}\text{O}_4$.

Sample	IS * (mm/s)	ΔE_{Q} (mm/s)	H_{hf} (T)	Site/Phase Assignment	Relative Areas (%)
CoFe_2O_4	0.374 ± 0.002	0.036 ± 0.038	5.75–46.44	H_{hf} distribution	92 ± 0.96
	0.361 ± 0.018	0.641 ± 0.037	-	Paramagnetic	8 ± 0.99
$\text{CoFe}_{1.8}\text{Er}_{0.2}\text{O}_4$	0.368 ± 0.002	0.012 ± 0.004	4.32–45.74	H_{hf} distribution	93 ± 1.0
	0.371 ± 0.016	0.916 ± 0.036	-	Paramagnetic	7 ± 1.02
$\text{CoFe}_{1.8}\text{Tb}_{0.2}\text{O}_4$	0.367 ± 0.002	0.022 ± 0.004	4.24–46.14	H_{hf} distribution	94 ± 0.98
	0.386 ± 0.021	0.603 ± 0.041	-	Paramagnetic	6 ± 1.01

* IS is given relative to α -iron.

A hyperfine magnetic field distribution from ~4 T to ~46 T reflects a rather wide particle size distribution as evidenced by TEM. A paramagnetic contribution represented by doublets with rather large line width in the central part of the spectrum, with abundance of 6–8%, is in rather good agreement with the amount of very small particles evidenced by the determined particle volume distribution. In the central quadrupole patterns the isomer shifts of the order of 0.37 mm/s are characteristics for Fe^{3+} in octahedral symmetry.

3.5. Magnetic Measurements

Figure 7 shows the magnetization curves (M – H) for $\text{CoFe}_{1.8}\text{Tb}_{0.2}\text{O}_4$ and $\text{CoFe}_{1.8}\text{Er}_{0.2}\text{O}_4$ at two different temperatures (5 and 300 K) and an applied magnetic field up to 5 T.

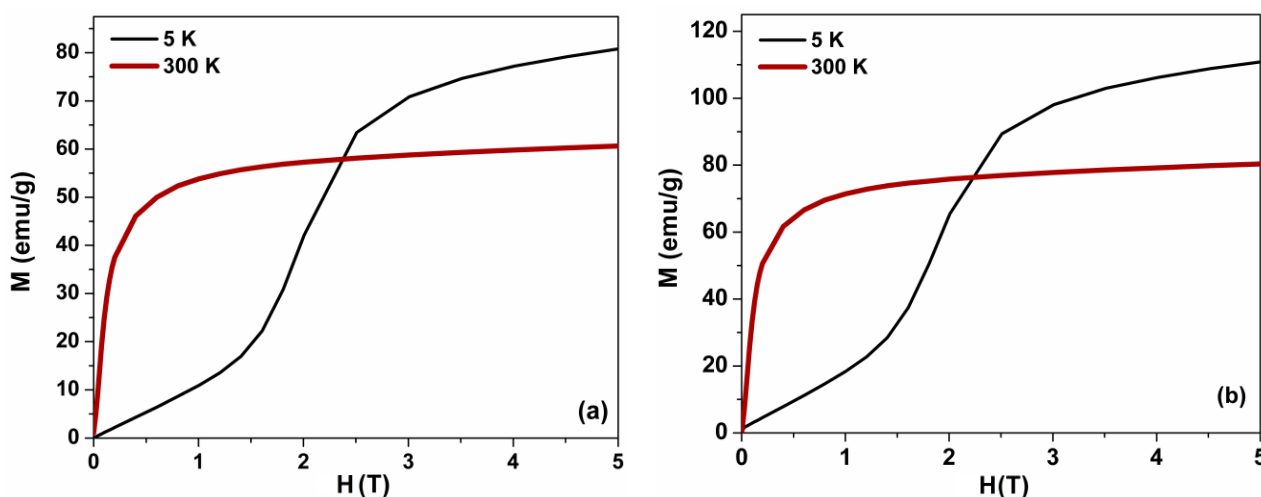


Figure 7. The M–H curves at 5 and 300 K for: (a) $\text{CoFe}_{1.8}\text{Tb}_{0.2}\text{O}_4$ sample; (b) $\text{CoFe}_{1.8}\text{Er}_{0.2}\text{O}_4$ sample.

Both samples show ferromagnetic behaviour. The M_s estimated at 300 K (~ 60 emu/g for $\text{CoFe}_{1.8}\text{Tb}_{0.2}\text{O}_4$, and ~ 80 emu/g for $\text{CoFe}_{1.8}\text{Er}_{0.2}\text{O}_4$) closely match with the previously reported values [10,36]. It can be observed that at ambient temperature, $\text{CoFe}_{1.8}\text{Tb}_{0.2}\text{O}_4$ has a saturation magnetization lower than that of the bulk CoFe_2O_4 ($M_s \approx 80$ emu/g) [41,42], while for $\text{CoFe}_{1.8}\text{Er}_{0.2}\text{O}_4$, the value of the saturation magnetization is similar. At low temperatures, the saturation magnetization values increase considerably (81 emu/g for the $\text{CoFe}_{1.8}\text{Tb}_{0.2}\text{O}_4$ sample and 110 emu/g for the $\text{CoFe}_{1.8}\text{Er}_{0.2}\text{O}_4$ sample, respectively). This behavior is due to the fact that at low temperatures, spin orientation thermal fluctuation can be neglected and the magnetic moments do not have enough energy to compete with the magnetic field.

Figure 7 reveals an interesting behavior of the magnetization curves as function of the applied magnetic field and temperature. At low magnetic field (less than 2.5 T), M–H curves show higher M values at higher temperature (300 K), while at higher magnetic field, M values are higher at low temperature (5 K). The reason for this behavior is the variation with temperature of the electronic population of hybrid orbitals. It is well established that the saturation magnetization of spinel ferrites depends on the degree of inversion. Additionally, the magnetic structure is sensitive to heat treatment of the sample.

On the other hand, the magnetic properties of rare earth doped CoFe_2O_4 ferrite strongly depend on the size and shape of the nanoparticles which are closely related to the method of preparation [33]. The magnetic behaviour of the samples consists in the formation of multiple magnetic domains generated by the cation distribution on the tetrahedral (A) and octahedral (B) sites.

This characteristic is confirmed by M–H curves at low temperatures where the slope changes are obvious. Normally, the cation distribution in substituted CoFe_2O_4 ferrite is $(\text{Fe}^{3+})_A[\text{Co}^{2+}_{1-x}\text{M}_x\text{Fe}^{3+}]_B\text{O}_4$. The super-exchange interactions (e.g., $\text{Fe}^{3+}(\text{B})\text{--O--Fe}^{3+}(\text{B})$, $\text{Fe}^{3+}(\text{B})\text{--O--Co}^{2+}(\text{B})$, $\text{Fe}^{3+}(\text{B})\text{--O--Fe}^{3+}(\text{A})$, $\text{Co}^{2+}(\text{B})\text{--O--Fe}^{3+}(\text{A})$, and $\text{Fe}^{3+}(\text{A})\text{--O--Fe}^{3+}(\text{A})$) is expected to be modified in RE^{3+} doped cobalt ferrite due to the appearance of $\text{RE}^{3+}\text{--Fe}^{3+}$ interactions (3d–4f coupling) [43,44]. The contribution to the M_s in $\text{CoFe}_{1.8}\text{Tb}_{0.2}\text{O}_4$ and $\text{CoFe}_{1.8}\text{Er}_{0.2}\text{O}_4$ can be interpreted in terms of rearrangement of cations in tetrahedral and octahedral sites, where some Co^{2+} ions can migrate to the tetrahedral sites by replacing an equivalent amount of Fe^{3+} ions from tetrahedral to octahedral sites. A wide range of experimental studies have shown that the magnetic properties of cobalt ferrite are affected by partial replacement of Fe^{3+} ions with various RE^{3+} ions [45–48]. Another factor that could induce changes in the magnetism of the two samples is the magnetic behaviour of RE^{3+} (both dopants have relatively high magnetic moments ~ 9.58 μB for Er^{3+} and ~ 9.72 μB for Tb^{3+}) and their distribution in the tetrahedral and octahedral sites [49]. The preferential tenancy of rare earth ions towards the octahedral sites in CoFe_2O_4 spinel

lattice will result in minimizing the number of Fe^{3+} ions at these sites and consequently the net magnetization will decrease. For both compositions, the total magnetic moments were calculated. The obtained values, 2.25 μB for Tb^{3+} doped CoFe_2O_4 , respectively, 2.67 μB for Er^{3+} doped CoFe_2O_4 are in agreement with those reported until now for the rare earth doped cobalt spinel ferrites, and very close to the theoretic magnetic moment of the CoFe_2O_4 (3 μB) [50,51]. Considering that, the magnetic properties of the RE^{3+} doped CoFe_2O_4 depend on the unpaired 4f electrons of RE ions [52], an increase in the $\text{CoFe}_{1.8}\text{Er}_{0.2}\text{O}_4$ magnetic moment is well justified.

3.6. Antimicrobial Activity

The tested compounds exhibited a higher efficiency against *P. aeruginosa* (MIC = MBEC = 0.125 mg mL^{-1}) and *E. faecalis* in planktonic growth (MIC = 0.5 mg mL^{-1}). For the other tested strains, higher MIC and MBEC values, of 1 mg mL^{-1} were recorded (Table 3).

Table 3. MIC and MBEC values of the tested nanoparticles against bacterial and fungal strains.

MIC	<i>S. aureus</i>	<i>E. faecalis</i>	<i>E. coli</i>	<i>P. aeruginosa</i>	<i>C. albicans</i>
$\text{CoFe}_{1.8}\text{Er}_{0.2}\text{O}_4$	1	0.5	1	0.125	1
$\text{CoFe}_{1.8}\text{Tb}_{0.2}\text{O}_4$	1	0.5	1	0.125	1
MBEC	<i>S. aureus</i>	<i>E. faecalis</i>	<i>E. coli</i>	<i>P. aeruginosa</i>	<i>C. albicans</i>
$\text{CoFe}_{1.8}\text{Er}_{0.2}\text{O}_4$	1	1	1	0.125	1
$\text{CoFe}_{1.8}\text{Tb}_{0.2}\text{O}_4$	1	1	1	0.125	1

The tested nanoparticles exhibited the same spectrum and intensity of the antimicrobial activity. Taking into account that the microbial biofilms are normally much more resistant to antimicrobial agents than their planktonic counterparts, requiring higher concentrations of active drugs, a very promising result is the fact that, exempting *E. faecalis*, the tested nanoparticles exhibited the same efficiency against planktonic and adhered bacteria [53].

The obtained results demonstrate the promising potential of the obtained nanoparticles for the development of antimicrobial applications, such as for the development of novel anti-biofilm agents or for the incorporation of the respective nanoparticles in different materials, in order to increase their resistance to microbial colonization and biofilm development, and therefore, to avoid the negative consequences of biofilm formation, in the industrial, ecological and medical fields.

4. Conclusions

The synthesis of Tb^{3+} and Er^{3+} substituted cobalt ferrites through wet ferritization method using temperatures below 100 °C leads to the formation of spinel oxide single phase. The lattice parameter a of the samples was found 8.3751 Å for $\text{CoFe}_{1.8}\text{Er}_{0.2}\text{O}_4$ and 8.3775 Å for $\text{CoFe}_{1.8}\text{Tb}_{0.2}\text{O}_4$. The inversion degree λ is 0.25 for $\text{CoFe}_{1.8}\text{Er}_{0.2}\text{O}_4$ while for $\text{CoFe}_{1.8}\text{Tb}_{0.2}\text{O}_4$, the presence of the larger Tb^{3+} ions leads to a normal spinel structure ($\lambda = 0$). The average particle size value (6.80 nm for $\text{CoFe}_{1.8}\text{Er}_{0.2}\text{O}_4$ and 5.91 nm for $\text{CoFe}_{1.8}\text{Tb}_{0.2}\text{O}_4$) estimated from the particle size distribution is close to the value of the average crystallite size (6.42 nm for $\text{CoFe}_{1.8}\text{Er}_{0.2}\text{O}_4$ and 5.77 nm for $\text{CoFe}_{1.8}\text{Tb}_{0.2}\text{O}_4$) calculated from the XRD data, which proves the single crystal nature of the particles. FTIR spectra sustained the formation of spinel ferrites. Mössbauer analysis evidenced the nanoparticle volume distribution in the analyzed samples via the hyperfine magnetic field distribution, highlighting the content of very small particles in the system. Both $\text{CoFe}_{1.8}\text{RE}_{0.2}\text{O}_4$ samples are ferromagnetic; the saturation magnetization (M_s) increases with temperature decreasing from 300 to 5 K. The M_s value at room temperature is ~60 emu/g for $\text{CoFe}_{1.8}\text{Tb}_{0.2}\text{O}_4$, and ~80 emu/g for $\text{CoFe}_{1.8}\text{Er}_{0.2}\text{O}_4$. The antimicrobial activity assays revealed a similar efficiency of the two types of $\text{CoFe}_{1.8}\text{RE}_{0.2}\text{O}_4$ ferrite nanoparticles against the tested Gram—positive and Gram-negative bacteria and fungal strains, both in planktonic and biofilm state. These results highlight the promising potential of these types of nanoparticles for the develop-

ment of novel anti-biofilm agents. Hence, this work shows the possibility of easily getting a wide variety of rare earth substituted spinel ferrites with a good control of phase purity and stoichiometry by a “chimie douce” process—the wet ferritization method.

Author Contributions: Conceptualization, D.G.; investigation, A.-C.I., L.D., V.-A.S., G.M., C.B., S.P., M.P. and M.C.C.; writing—original draft, D.G., I.M., A.-C.I., L.D., G.M., C.B. and M.C.C.; writing—review and editing, D.G. and I.M.; supervision, D.G. and I.M. All authors have read and agreed to the published version of the manuscript.

Funding: This research received no external funding.

Acknowledgments: D. Gingasu and I. Mindru would like to thank. Luminita Patron for her support and expertise.

Conflicts of Interest: The authors declare no conflict of interest.

References

1. Kefeni, K.K.; Msagati, T.A.M.; Mamba, B.B. Ferrite nanoparticles: Synthesis, characterization and applications in electronic device. *Mat. Sci. Eng. B* **2017**, *215*, 37–55. [[CrossRef](#)]
2. Won, S.; Kim, S.; Park, J.E.; Jeon, J.; Wie, J.J. On-demand orbital maneuver of multiple soft robots via hierarchical magnetomotility. *Nat. Commun.* **2019**, *10*, 4751. [[CrossRef](#)] [[PubMed](#)]
3. Carpenter, J.A.; Eberle, T.B.; Schuerle, S.; Rafsanjani, A.; Studart, A.R. Facile Manufacturing Route for Magneto-Responsive Soft Actuators. *Adv. Intell. Syst.* **2021**, *3*, 2000283. [[CrossRef](#)]
4. Shobana, M.K. Nanoferrites in biosensors—A review. *Mat. Sci. Eng. B* **2021**, *272*, 115344. [[CrossRef](#)]
5. Kim, D.-H.; Nikles, D.E.; Johnson, D.T.; Brazel, C.S. Heat generation of aqueously dispersed CoFe_2O_4 nanoparticles as heating agents for magnetically activated drug delivery and hyperthermia. *J. Magn. Magn. Mater.* **2008**, *320*, 23–209. [[CrossRef](#)]
6. De, D.; Upadhyay, P.; Das, A.; Ghosh, A.; Adhikary, A.; Goswami, M.M. Studies on cancer cell death through delivery of dopamine as anti-cancer drug by a newly functionalized cobalt ferrite nano-carrier. *Colloids Surf. A Physicochem. Eng. Asp.* **2021**, *627*, 127202. [[CrossRef](#)]
7. Arshad, J.M.; Raza, W.; Amin, N.; Nadeem, K.; Arshad, M.I.; Khan, M.A. Synthesis and characterization of cobalt ferrites as MRI contrast agent. *Mater. Today Proc.* **2021**, *47*, S50–S54. [[CrossRef](#)]
8. Manohar, A.; Geleta, D.D.; Krishnamoorthi, C.; Lee, J. Synthesis, characterization and magnetic hyperthermia properties of nearly monodisperse CoFe_2O_4 nanoparticles. *Ceram. Int.* **2020**, *46*, 28035–28041. [[CrossRef](#)]
9. Nikumbh, A.K.; Pawar, R.A.; Nighot, D.V.; Gugale, G.S.; Sangale, M.D.; Khanvilkar, M.B.; Nagawade, A.V. Structural, electrical, magnetic and dielectric properties of rare-earth substituted cobalt ferrites nanoparticles synthesized by the co-precipitation method. *J. Magn. Magn. Mater.* **2014**, *355*, 201–209. [[CrossRef](#)]
10. Zhao, L.; Yang, H.; Zhao, X.; Yu, L.; Cui, Y.; Feng, S. Magnetic properties of CoFe_2O_4 ferrite doped with rare earth ion. *Mater. Lett.* **2006**, *60*, 1–6. [[CrossRef](#)]
11. Murugesan, C.; Chandrasekaran, G. Impact of Gd^{3+} -substitution on the structural, magnetic and electrical properties of cobalt ferrite nanoparticles. *RSC Adv.* **2015**, *5*, 73714–73725. [[CrossRef](#)]
12. Ateia, E.E.; Abdelmaksoud, M.K.; Arman, M.M.; Shafaay, A.S. Comparative study on the physical properties of rare-earth-substituted nano-sized CoFe_2O_4 . *Appl. Phys. A* **2020**, *126*, 91. [[CrossRef](#)]
13. Almessiere, M.A.; Slimani, Y.; Korkmaz, A.D.; Guner, S.; Sertkol, M.; Shirsath, S.E.; Baykal, A. Structural, optical and magnetic properties of Tm^{3+} substituted cobalt spinel ferrites synthesized via sonochemical approach. *Ultrason. Sonochem.* **2019**, *54*, 1–10. [[CrossRef](#)] [[PubMed](#)]
14. Prathapani, S.; Vinitha, M.; Jayaraman, T.V.; Das, D. Effect of Er doping on the structural and magnetic properties of cobalt-ferrite. *J. Appl. Phys.* **2014**, *115*, 17A502. [[CrossRef](#)]
15. Maksoud, M.I.A.A.; El-Sayyad, G.S.; Ashour, A.H.; El-Batal, A.I.; Elsayed, M.A.; Gobara, M.; El-Khawaga, A.M.; Abdel-Khalek, E.K.; El-Okr, M.M. Antibacterial, antibiofilm, and photocatalytic activities of metals-substituted spinel cobalt ferrite nanoparticles. *Microb. Pathog.* **2019**, *127*, 144–158. [[CrossRef](#)]
16. Chifiriuc, C.; Lazar, V.; Bleotu, C.; Calugarescu, I.; Grumezescu, A.M.; Mihaiescu, D.E.; Mogosanu, D.E.; Buteica, A.S.; Buteica, E. Bacterial adherence to the cellular and inert substrate in the presence of CoFe_2O_4 and Fe_3O_4 /oleic acid-core/shell. *Dig. J. Nanomater. Bios.* **2011**, *6*, 37–42.
17. Gingasu, D.; Mindru, I.; Mocioiu, O.C.; Preda, S.; Stanica, N.; Patron, L.; Ianculescu, A.; Oprea, O.; Nita, S.; Paraschiv, I.; et al. Synthesis of nanocrystalline cobalt ferrite through soft chemistry methods: A green chemistry approach using sesame seed extract. *Mater. Chem. Phys.* **2016**, *182*, 219–230. [[CrossRef](#)]
18. Gingasu, D.; Mindru, I.; Patron, L.; Calderon-Moreno, J.M.; Mocioiu, O.C.; Preda, S.; Stanica, N.; Nita, S.; Dobre, N.; Popa, M.; et al. Green synthesis methods of CoFe_2O_4 and $\text{Ag-CoFe}_2\text{O}_4$ nanoparticles using hibiscus extracts. *J. Nanomater.* **2016**, *2016*, 2106756. [[CrossRef](#)]

19. Naik, M.M.; Naik, H.S.B.; Nagaraju, G.; Vinuth, M.; Vinu, K.; Viswanath, R. Green synthesis of zinc doped cobalt ferrite nanoparticles: Structural, optical, photocatalytic and antibacterial studies. *Nano-Struct. Nano-Objects* **2019**, *19*, 100322. [[CrossRef](#)]
20. Demirci, Ç.E.; Manna, P.K.; Wroczynski, Y.; Aktürk, S.; van Lierop, J. Lanthanum ion substituted cobalt ferrite nanoparticles and their hyperthermia efficiency. *J. Magn. Magn. Mater.* **2018**, *458*, 253–260. [[CrossRef](#)]
21. Koutsoubou, X.; Tsiaoussis, I.; Bulai, G.A.; Caltun, O.F.; Kalogirou, O.; Sarafidis, C. $\text{CoFe}_{2-x}\text{RE}_x\text{O}_4$ (RE=Dy, Yb, Gd) magnetic nanoparticles for biomedical applications. *Phys. B* **2021**, *606*, 412849. [[CrossRef](#)]
22. Žalneravičius, R.; Paškevičius, A.; Kurtinaitiene, M.; Jagminas, A. Size-dependent antimicrobial properties of the cobalt ferrite nanoparticles. *J. Nanopart. Res.* **2016**, *18*, 300. [[CrossRef](#)]
23. Elayakumar, K.; Dinesh, A.; Manikandan, A.; Palanivelu, M.; Kavitha, G.; Prakash, S.; Kumar, R.T.; Jaganathan, S.K.; Baykal, A. Structural, morphological, enhanced magnetic properties and antibacterial bio-medical activity of rare earth element (REE) Cerium (Ce^{3+}) doped CoFe_2O_4 nanoparticles. *J. Magn. Magn. Mater.* **2019**, *476*, 157–165. [[CrossRef](#)]
24. Ben Tahar, J.L.; Artus, M.; Ammar, S.; Smiri, L.S.; Herbst, F.; Vaulay, M.-J.; Richard, V.; Grenèche, J.-M.; Villain, F.; Fiévet, F. Magnetic properties of $\text{CoFe}_{1.9}\text{RE}_{0.1}\text{O}_4$ nanoparticles (RE = La, Ce, Nd, Sm, Eu, Gd, Tb, Ho) prepared in polyol. *J. Magn. Magn. Mater.* **2008**, *320*, 643–646. [[CrossRef](#)]
25. Wu, X.; Ding, Z.; Song, N.; Li, L.; Wang, W. Effect of the rare-earth substitution on the structural, magnetic, and adsorption properties in cobalt ferrite nanoparticles. *Ceram. Int.* **2016**, *42*, 4246–4255. [[CrossRef](#)]
26. Sumalatha, E.; Nyathani, M.; Babu, T.A.; Ravinder, D.; Prasad, N.V.K.; Katlakunta, S. Eco-Friendly Synthesis, TEM and Magnetic Properties of Co-Er Nano-Ferrites. *Biointerface Res. Appl. Chem.* **2022**, *12*, 910–928. [[CrossRef](#)]
27. Sugimoto, T.; Matijevic, E. Formation of uniform spherical magnetite particle by crystallization from ferrous hydroxide gels. *J. Colloid Interf. Sci.* **1980**, *74*, 227–243. [[CrossRef](#)]
28. Ferreira, T.A.S.; Waerenborgh, J.C.; Mendonça, M.H.R.M.; Nunes, M.R.; Costa, F.M. Structural and morphological characterization of FeCo_2O_4 and CoFe_2O_4 spinels prepared by a coprecipitation method. *Solid State Sci.* **2003**, *5*, 383–392. [[CrossRef](#)]
29. O'Neill, H.; Navrotsky, A. Simple spinels: Crystallographic parameters, cation radii, lattice energies, and cation distribution. *Am. Mineral.* **1983**, *68*, 181–194.
30. Shannon, R.D. Revised effective ionic radii and systematic studies of interatomic distances in halides and chalcogenides. *Acta Cryst. A* **1976**, *32*, 751–767. [[CrossRef](#)]
31. Prodan, A.M.; Iconaru, S.L.; Ciobanu, C.S.; Chifiriuc, M.C.; Stoicea, M.; Predoi, D. Iron oxide magnetic nanoparticles: Characterization and toxicity evaluation by in vitro and in vivo assays. *J. Nanomater.* **2013**, *2013*, 587021.
32. Kakade, S.G.; Ma, Y.-R.; Devan, R.S.; Kolekar, Y.D.; Ramana, C.V. Dielectric, complex impedance, and electrical transport properties of erbium (Er^{3+}) ion-substituted nanocrystalline, cobalt-rich ferrite ($\text{Co}_{1.1}\text{Fe}_{1.9-x}\text{Er}_x\text{O}_4$). *J. Phys. Chem. C* **2016**, *120*, 5682–5693. [[CrossRef](#)]
33. Cheng, F.-X.; Jia, J.-T.; Xu, Z.-G.; Zhou, B.; Liao, C.-S.; Yan, C.-H. Microstructure, magnetic, and magneto-optical properties of chemical synthesized Co-RE (RE = Ho, Er, Tm, Yb, Lu) ferrite nanocrystalline films. *J. Appl. Phys.* **1999**, *86*, 2727–2732. [[CrossRef](#)]
34. Zhang, Y.; Wen, D. Influence of RE/Mn (RE = La, Nd and Gd) ratios on the infrared absorption and emission properties of Co-Zn ferrites. *Adv. Mater. Res.* **2011**, *217–218*, 311–316. [[CrossRef](#)]
35. Naik, S.R.; Salker, A.V. Change in the magnetostructural properties of rare earth doped cobalt ferrites relative to the magnetic anisotropy. *J. Mater. Chem.* **2012**, *22*, 2740–2750. [[CrossRef](#)]
36. Prathapani, S.; Jayaraman, T.V.; Varaprasadarao, E.K.; Das, D. Structural and ambient/sub-ambient temperature magnetic properties of Er-substituted cobalt-ferrites synthesized by sol-gel assisted auto-combustion method. *J. Appl. Phys.* **2014**, *116*, 023908. [[CrossRef](#)]
37. Khana, A.; Javid ur Rehman, M.; Mahmood, K.; Ali, I.; Akhtar, M.N.; Murtaza, G.; Shakir, I.; Warsig, M.F. Impacts of Tb substitution at cobalt site on structural, morphological and magnetic properties of cobalt ferrites synthesized via double sintering method. *Ceram. Int.* **2015**, *41*, 2286–2293. [[CrossRef](#)]
38. Gharibshahian, M.; Mirzaee, O.; Nourbakhsh, M.S. Evaluation of superparamagnetic and biocompatible properties of mesoporous silica coated cobalt ferrite nanoparticles synthesized via microwave modified Pechini method. *J. Magn. Magn. Mater.* **2017**, *425*, 48–56. [[CrossRef](#)]
39. Greenwood, N.N.; Gibb, T.C. *Mössbauer Spectroscopy*; Chapman and Hall Ltd.: London, UK, 1971.
40. Fock, J.; Hansen, M.F.; Frandsen, C.; Mørup, S. On the interpretation of Mössbauer spectra of magnetic nanoparticles. *J. Magn. Magn. Mater.* **2018**, *445*, 11–21. [[CrossRef](#)]
41. Duong, G.V.; Hanh, N.; Linh, D.V.; Groessinger, R.; Weinberger, P.; Schafner, E.; Zehetbauer, M. Monodispersed nanocrystalline $\text{Co}_{1-x}\text{Zn}_x\text{Fe}_2\text{O}_4$ particles by forced hydrolysis: Synthesis and characterization. *J. Magn. Magn. Mater.* **2007**, *311*, 46–50. [[CrossRef](#)]
42. Gözüak, F.; Köseoğlu, Y.; Baykal, A.; Kavas, H. Synthesis and characterization of $\text{Co}_x\text{Zn}_{1-x}\text{Fe}_2\text{O}_4$ magnetic nanoparticles via a PEG-assisted route. *J. Magn. Magn. Mater.* **2009**, *321*, 2170–2177. [[CrossRef](#)]
43. Manova, E.; Kunev, B.; Paneva, D.; Mitov, I.; Petrov, L.; Estournès, C.; D'Orleans, C.; Rehspringer, J.L.; Kurmoo, M. Mechano-synthesis, characterization, and magnetic properties of nanoparticles of cobalt ferrite, CoFe_2O_4 . *Chem. Mater.* **2004**, *16*, 5689–5696. [[CrossRef](#)]
44. Tripathy, D.; Adeyeye, A.O.; Boothroyd, C.B.; Piramanayagam, S.N. Magnetic and transport properties of Co-doped Fe_3O_4 films. *J. Appl. Phys.* **2007**, *101*, 013904. [[CrossRef](#)]

45. Cheng, F.; Liao, C.; Kuang, J.; Xu, Z.; Yana, C.; Chen, L.; Zhao, H.; Liu, Z. Nanostructure magneto-optical thin films of rare earth (RE=Gd, Tb, Dy) doped cobalt spinel by sol-gel synthesis. *J. Appl. Phys.* **1999**, *85*, 2782–2786. [[CrossRef](#)]
46. Kahn, M.L.; Zhang, Z.J. Synthesis and magnetic properties of CoFe₂O₄ spinel ferrite nanoparticles doped with lanthanide ions. *Appl. Phys. Lett.* **2001**, *78*, 3651–3653. [[CrossRef](#)]
47. Panda, R.N.; Shih, J.C.; Chin, T.S. Magnetic properties of nano-crystalline Gd- or Pr-substituted CoFe₂O₄ synthesized by the citrate precursor technique. *J. Magn. Magn. Mater.* **2003**, *257*, 79–86. [[CrossRef](#)]
48. Peng, J.; Hojamberdiev, M.; Xu, Y.; Cao, B.; Wang, J.; Wu, H. Hydrothermal synthesis and magnetic properties of gadolinium-doped CoFe₂O₄ nanoparticles. *J. Magn. Magn. Mater.* **2011**, *323*, 133–137. [[CrossRef](#)]
49. Frazer, B.H.; Gebhardt, J.R.; Ali, N. Magnetic phase diagrams of erbium. *J. Appl. Phys.* **1999**, *85*, 6100–6102. [[CrossRef](#)]
50. Reddy, R.A.; Rao, K.R.; Babu, B.R.; Kumar, G.K.; Rajesh, C.; Chatterjee, A.; Jyothi, N.K. Structural, electrical and magnetic properties of cobalt ferrite with Nd³⁺ doping. *Rare Met.* **2022**, *41*, 240–245. [[CrossRef](#)]
51. Szotek, Z.; Temmerman, W.M.; Ködderitzsch, D.; Svane, A.; Petit, L.; Winter, H. Electronic structures of normal and inverse spinel ferrites from first principles. *Phys. Rev. B* **2006**, *74*, 174431. [[CrossRef](#)]
52. Hou, Y.H.; Huang, Y.L.; Hou, S.J.; Ma, S.C.; Liu, Z.W.; Ouyang, Y.F. Structural, electronic and magnetic properties of RE³⁺-doping in CoFe₂O₄: A first-principles study. *J. Magn. Magn. Mater.* **2017**, *421*, 300–305. [[CrossRef](#)]
53. Telcian, A.; Mohammed, D.H.; Chifiriuc, M.C.; Bleotu, C.; Holban, A.M.; Curutiu, C.; Grosu, E.; Ficai, A.; Mihaescu, G.; Grigore, R.; et al. Assessment of the anti-biofilm activity and biocompatibility of novel PE and PVC polymers. *Rom. Biotech. Lett.* **2017**, *22*, 12997–13004.